A high frequency model for predicting the behavior of lithium-ion batteries connected to fast switching power electronics

Pablo Korth Pereira Ferraz[a,*], Robert Schmidt[a,b], Delf Kober[c], Julia Kowal[a]

[a] Electrical Energy Storage Technology (EET), Department of Energy and Automation, Technische Universität Berlin, Einsteinufer 11, D-10587 Berlin, Germany
[b] Power System Engineering, Bergische Universität Wuppertal, Rainer-Grünter-Str. 21, D-42119 Wuppertal, Germany
[c] Chair of Advanced Ceramic Materials, Institut für Werkstoffwissenschaften und -technologien, Technische Universität Berlin, Hardenbergstr. 40, D-10623 Berlin, Germany

ARTICLE INFO

ABSTRACT

Battery powered energy systems such as electric vehicles utilize power electronics for controlling energy flows between the battery and the load or generation, respectively. Therefore, the battery is under high frequency stress due to fast switching power electronic devices. However, most battery models throughout the literature are not able to cope with high frequency excitation. This paper proposes an easy to implement equivalent circuit model that covers aforementioned frequency regions with a series of inductors that are each connected in parallel with an ohmic resistance. This circuit is parameterized by electrochemical impedance spectroscopy (EIS) up to 100 kHz. For further regions that reach regions of megahertz a skin effect model is investigated and compared to the *RL*-model. It is shown that such semi-empirical models can be motivated by geometrical considerations that can be found in the literature. Moreover, the proposed model is validated by simulating the voltage response from an input current that originates from an actual back-to-back half bridge DC/DC converter. The promising results indicate that such models might be implemented in future battery energy systems to improve insights on how batteries react to perturbations such as EMI noise or high frequency current ripple.

1. Introduction

It is commonly accepted that lithium-ion batteries are going to be a crucial factor for the energy transition from fossil fuels towards renewable energies regarding either the necessity to buffer fluctuating feed-ins from solar and wind power plants, improving grid quality and grid stability or as one feasible energy storage for electric mobility [1,2]. Given that distributed generation is an immanent feature of renewable energies, a paradigm shift towards new forms of electrical energy networks such as microgrids [3] has been initiated and batteries are commonly seen as a self-evident part of such smaller scaled networks to guarantee uninterrupted service or increase the degree of utilization of renewable power plants [4]. One example is to equip electric cars with back-to-back battery chargers [5] instead of the nowadays widely used unidirectional vehicle battery chargers [6] so that the car's traction battery can be used as a backup storage which is known as the concept "vehicle to grid" (V2G) [7,8].

Regardless of all the aforementioned ideas being future concepts or already commercially available, they have one vital similarity: The design of energy systems cannot be done without taking power electronics into account. In principle, power electronic devices convert a mostly arbitrary current or voltage signal into another with power switches such as field-effect transistors (FET) or insulated gate bipolar transistors (IGBT) that are turned on and off periodically, e.g. controlled by pulse-width modulation (PWM) [9]. The switching frequency is within the magnitude of several kilohertz and therefore induces high-frequency noise and current ripple as shown for a half bridge based DC/DC converter in Fig. 1.

Thus, batteries that are connected to power electronics face high-frequency excitation. Therefore, a novel model that is able to represent a battery's high-frequency behavior with a satisfactory explanation for its elements needs to be developed. In order to achieve a model that is easy to parameterize and is potentially simple enough to be implemented in online battery monitoring systems without inducing too much computational burden [10], two well established methods for modeling and parameterizing batteries, respectively, have been chosen. In this work, electrochemical impedance spectroscopy (EIS) is used to measure the voltage response due to a harmonic input current to calculate the cell's impedance which is then passed to a fitting algorithm so that an equivalent circuit model can be implemented [11]. In the past, this practice has been discussed thoroughly in the literature, e.g. in [12–14]. Yet, only a few researchers have dealt with models that take

---

* Corresponding author.
  E-mail address: pablo.korthpereiraferraz@tu-berlin.de (P. Korth Pereira Ferraz).

(a) Typical current wave form of a DC/DC-converter
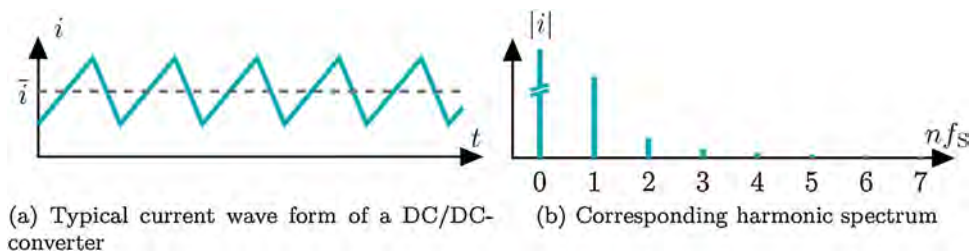
(b) Corresponding harmonic spectrum

Fig. 1. The left side shows a qualitative diagram of a typical battery current waveform if connected to a DC/DC-converter, e.g. a boost converter. On the right side, the corresponding harmonic spectrum is shown qualitatively, too. It declines in orders of $1/n^2$.
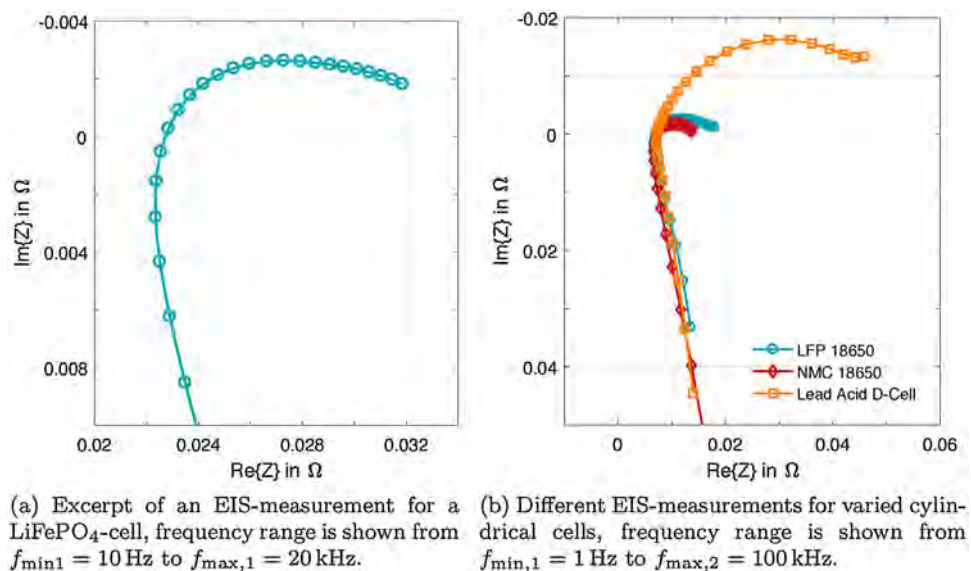

(a) Excerpt of an EIS-measurement for a LiFePO$_4$-cell, frequency range is shown from $f_{\min 1} = 10\,\text{Hz}$ to $f_{\max,1} = 20\,\text{kHz}$.

(b) Different EIS-measurements for varied cylindrical cells, frequency range is shown from $f_{\min,1} = 1\,\text{Hz}$ to $f_{\max,2} = 100\,\text{kHz}$.

Fig. 2. Exemplary impedance spectra clearly show significant growth of the real part for high frequencies for various cylindrical cells.

the inductive branch, i.e. the high-frequency behavior, into account. In [15,16] and to some extent [17] an impedance analysis with high-frequency excitation has been undertaken and an inductance in parallel to an ohmic resistance is proposed as an equivalent circuit model. Their conclusions are motivated by an increasing real part at high frequencies, as illustrated in Fig. 2, which seems to be imminent for a lot of cell technologies, since a regrowth of the real part at higher frequencies has been observed in the past and is clearly visible for every measurement throughout this work. However, a deep analysis is missing in the literature. Moreover, it is established to provide aforementioned inductive equivalent circuits to achieve an exceedingly precise fitting result but neglecting them in the following simulation for reasons concerning simulation stability [18].

Further battery models that are based on transmission line approaches are also discussed. In case of [19], the effect of EMI on the battery is investigated so that its primary frequency range is by far higher than a typical switching frequency of power electronics, which normally operates in the range of several kilohertz. The authors of [20] provide a more promising concept for a lower band which is based on the geometrical concept of a spiral-wound cell [21]. Therefore, another goal of this work is to provide an equivalent circuit model that is usable in simulations of power electronic battery systems as it uses *RL*-circuits not only in terms of an improved parameterization but as a key part of the simulation as well. With this modeling approach, a more precise prediction of the battery's voltage response due to high frequency current ripple is achieved.

In Section 2 the carried out electrochemical impedance measurements are presented. It is followed by the modeling approach with an equivalent circuit and its parameterization in Section 3. Afterwards, the developed model is evaluated and discussed in Section 4 as it is tested

with measurement data of a real life battery system, based on a half-bridge DC/DC converter.

2. Experimental

2.1. Cell characteristics and equipment used

All measurements presented in this work are done with commercial spiral wound cylindrical cells with varying chemistry, see Fig. 2b. Albeit the proposed model has been derived for any given cylindrical cell, only a 18,650 spiral wound cylindrical high power lithium-ion cell is investigated further to focus on the properties of the model. The anode consists of graphite and the cathode is made of lithium iron phosphate (LFP). The nominal properties of the identical cells are listed in Table 1. They are both cycled and characterized by a *Zahner Zennium* impedance spectroscope. This device has also been used to conduct the EIS-measurements. The cells are connected in a way to utilize four-terminal sensing. The wires for voltage and current are twisted in pairs respectively to minimize the stray effects. Ultimately, the cells are tested in a *Binder MK 240* climate chamber.

Table 1
Nominal features of the battery under test.

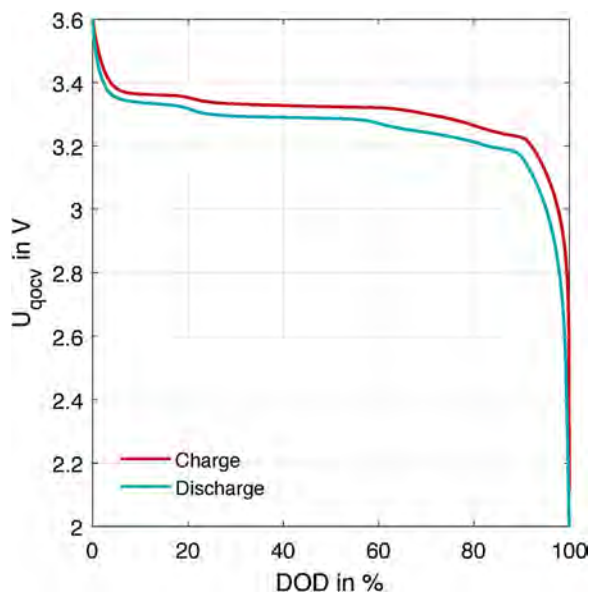| Value	Symbol	Quantity
Nominal capacity	C_N	1, 1 A h
Nominal voltage	U_N	3, 3 V
End-of-charge voltage	U_{EoC}	3, 6 V
Cutoff voltage	U_{CO}	2 V

Fig. 3. Terminal voltage measurements for the given LFP-cell at $C/40$ current rate to represent phase transitions and voltage hysteresis between charge and discharge. (For interpretation of the references to color in this figure citation, the reader is referred to the web version of this article.)

2.2. Results

To obtain the curves in Fig. 3, the fully charged battery has been discharged between U_{EoC} and U_{CO} with a current-rate of $C/40$ to get the lower of the two curves, marked in blue. At the time when the battery has hit U_{CO}, it has been charged again until U_{EoC} with the same current-rate to obtain the upper red line. Both curves should be as close to their respective open circuit voltage (OCV) as possible since overpotentials may be neglected when using such low current rates [22]. Thus, the voltage curves in Fig. 3 are used as a time-saving approximation instead of an OCV curve.

EIS-measurements have been done at each combination of state of charge (SOC) and temperature, given in Table 2. The cells have been excited galvanostatically with an amplitude of 50 mA and without any underlaid constant current component. To ensure minimal parameter variance, e.g. aging processes due to severe temperature conditions, a new cell of the same batch has been used for each temperature. At each SOC listed in Table 2, an EIS-measurement has been conducted after a partial charge and after a partial discharge, respectively. Thus, every cell has undergone 14 EIS measurements. After each partial charge/discharge the cell has been relaxated for four hours to ensure that relaxation processes do not interfere with the actual measurement [23]. The frequency range of the EIS-measurements has been set to $f_{EIS} \in [1\,\text{Hz } 1\,\text{MHz}]$ to cover typical switching frequencies of power electronic converters and sufficient parts of their harmonic spectrum. For illustrative purposes, the frequency ranges that are shown in the following diagrams are adapted accordingly.

The essential results of the EIS measurement are depicted in Figs. 4 and Figure 5. Each Nyquist plot is cut off at $f_{co} = 100\,\text{kHz}$ so that the inductive branch appears shorter, thus leaving the capacitive area and the cross section with the real axis at lower frequencies visible. The starting frequencies range from $f_{SL} = 1\,\text{Hz}$ to $f_{SH} = 100\,\text{Hz}$, depending on temperature and SOC. This range is chosen so that the measurement

Table 2
Test conditions for EIS-measurements.

Temperature in °C	−20	−10	0	10	20	40	55
State of charge (SOC) in %	0	10	30	50	70	90	100

frequencies are in the range of typical switching frequencies of power electronics in the range of several kilohertz. Besides, a differentiation between charge and discharge is neglected since the deviations between the corresponding impedance measurements are comparatively small. Therefore, only the spectra after a discharge pulse are shown.

In Fig. 4, four exemplary temperatures to represent Table 2 are chosen and the impedance is plotted for each SOC. Except for the lower frequency region and there especially SOC = 0, the curves are similar and show no significantly different behavior. Moreover, each plot shows a curvature in the inductive branch which leads to the conclusion that the increase of the ohmic resistance is not purely linear. Taking Fig. 5 into account, those observations are further supported. Each graph shows a different SOC and the corresponding curves at the temperatures listed in Table 2. As expected, a lower temperature such as −20 °C, −10 °C or 0 °C leads to a lower ion conductivity and therefore results in a significantly higher inner resistance that can be estimated as the intersection of the real axis. The unexpected shift of the light blue and square marked curve, measured at 40 °C, is most likely linked to the variation of cell parameters since a different cell has been used for each temperature. Furthermore, it is bent more than the graphs at lower temperatures. This can be generally noted: The higher the temperature, the more compressed the first capacitive semicircle appears as it can be seen in the details in Fig. 5. This corresponds with the second row of Table 3 as the point of intersection is directly linked to the first depressed semicircle in the capacitive half-plane because double layer capacitive effects are defined by the law of Debye and Hückel [24].

The first two rows of Table 3 are the aforementioned frequency f_{IS} and resistance R_{IS} at the intersection that are subject to temperature, respectively. They are followed by the relative increase of the real part ΔR_i, measured at 100 kHz and at 1 MHz. Those measurements can be seen as "how far" the inductive branch has been bent towards higher real parts and how it develops over the given frequency domain. As the ohmic changes $\Delta R_{100\,\text{kHz}}$ and $\Delta R_{1\,\text{MHz}}$ are related to each respective intersection, a slight connection between temperature and the real part at high frequencies is observed, for the real part rises more at higher temperatures. The effect is more visible for $\Delta R_{100\,\text{kHz}}$ as it is for $\Delta R_{1\,\text{MHz}}$. Yet, this is not distinctive enough to be investigated deeper within the scope of this work. However, especially when it comes to the resistive rise until 100 kHz, it has to be noted that the behavior at high frequencies is influenced by the battery's capacitive parts so that those need to be taken into account in an electric model, too. This is shown in more detail in Section 3.

In the last row, the imaginary part at 1 MHz has been approximated as an inductance, calculated by $\text{Im}\{\underline{Z}\}_{1\,\text{MHz}} \approx j\omega L_{1\,\text{MHz}}$ to give an impression at which orders of magnitude the inductive behavior of a spiral-wound 18,650 lithium-ion battery is located. The given range and its independence from temperature clearly indicates that the inductive part is mainly affected by wiring and the cell's geometry.

3. Modeling

In the past, equivalent circuit models have been thoroughly investigated. Yet, the inductive behavior has mostly been modeled by a simple series inductor, e.g. in [12,25], or has been neglected [26]. The results shown in Section 2.2 and recent studies [18] clearly indicate that this is insufficient for a comprehensive model that is also capable of simulating the battery's behavior under high-frequency excitation because they cannot cope with the consistently observed rise of the real part in the positive half-plane. Besides, the measurements suggest that the ohmic-inductive characteristic at higher frequencies are hardly influenced by the SOC and do not show significant correlations to temperature variations. Therefore, a strong dependence on the geometry of the cell and the wiring is assumed. This has been stated before without any further reason, e.g. in [27] and has been rigorously investigated in [20]. It is based on the assumption that spiral wound cells are basically
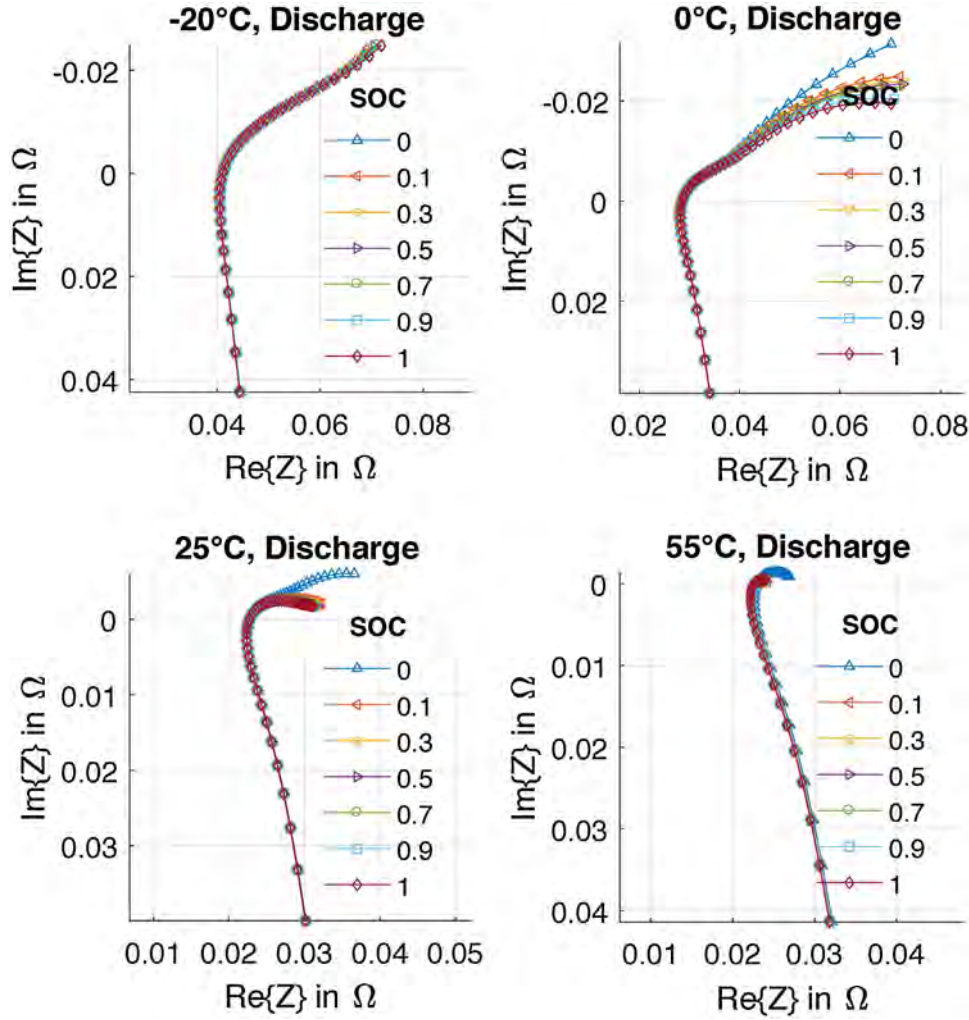
Fig. 4. Measurement results, summarized for same temperatures with a shown measurement range from $f_{EIS} \in [1\,\text{Hz}\ 100\,\text{kHz}]$.

a parallel connection of a large number of fractional cells connected by the current collectors which are modeled by differential ohmic resistances and a differential inductors. Albeit generating satisfactory replications, the proposed model in [20] needs 38 independent parameters that are computed by complex geometrical equations for spiral-wound cells as in [21]. This approach requires knowledge of the cell's inner dimensions which are often unknown. Thus, a more practical approach is to approximate the complex network of small but numerous resistive and inductive parts with a simpler network that is an empirical description of the fractional modeling of the current collectors. Consequently, the proposed model does not need profound knowledge of the cell's geometry as it is completely parameterizable by impedance measurements.

A closer look at, for example, Fig. 2 reveals a convoluted curve in the positive imaginary half-plane which is congruent with earlier research, as in [15,16,18,28,29]. Therefore, an "inductive constant phase element" (CPE) is proposed. Its impedance is

$$\underline{Z}_{\text{CPE,ind}} = (j\omega)^{\xi_L} \widetilde{L} = A_L e^{j\pi/(2\xi_L)} \qquad (1)$$

with $\omega^{\xi_L} \widetilde{L} = A_L$, the complex number j, the angular frequency ω and the inductance $\widetilde{L}$. The tilde is used to indicate that $\widetilde{L}$ is not purely inductive since its unit is $[\widetilde{L}] = \text{Hs}^{\xi_L}$. As ξ_L induces fractional order differential equations [30], the implementation of the proposed model in tools such as *MATLAB/Simulink* becomes rather difficult. Therefore, in full analogy to the well-known practice in the low-frequency region, the inductive CPE is approximated with m RL-circuits as shown in the upper

half of Fig. 6.

Taking a look back at Table 3 indicates that the cross section of the real axis is dependent on temperature and reaches regions of possible switching frequencies of power electronics. Therefore, the capacitive part cannot be neglected and is measured down to $f_{\text{SL}} = 1\,\text{Hz}$ so that the first semicircle is completely covered even at higher temperatures, see Fig. 4. It is widely recognized that the depressed semicircle can be described by a ZARC-element, consisting of a capacitive constant phase element and a resistor in parallel [12,25,27]. For the same reasons mentioned above, a ZARC-element is also difficult to implement and thus described by n RC-circuits instead, see the lower part of Fig. 6.

The full model is thereby written as

$$\underline{Z} = R_i + \underbrace{\sum_{i=1}^{m} \frac{j\omega L_i}{1 + j\omega(L_i/R_{L_i})}}_{\underline{Z}_{Z,\text{ind}}} + \underbrace{\sum_{i=1}^{n} \frac{R_{C_i}}{1 + j\omega C_i R_{C_i}}}_{\underline{Z}_Z}. \qquad (2)$$

In this work, choosing $m = 3$ and $n = 5$ as parameters has delivered satisfactory results. Four examples for two different SOC and two different temperatures are shown in Fig. 7. Only minimal deviations are observable which are verified by the normalized root mean square error

$$\text{NRMSE} = \frac{\sqrt{(|\underline{Z}|_{\text{meas}} - |\underline{Z}|_{\text{calc}})^2/N}}{\overline{|\underline{Z}|}_{\text{meas}}} \qquad (3)$$

because it does not exceed the range of low single digit percentages for any measurement and is way below 0.5% at most times. Moreover, the deviations rise from the low frequency part as the equivalent circuit in
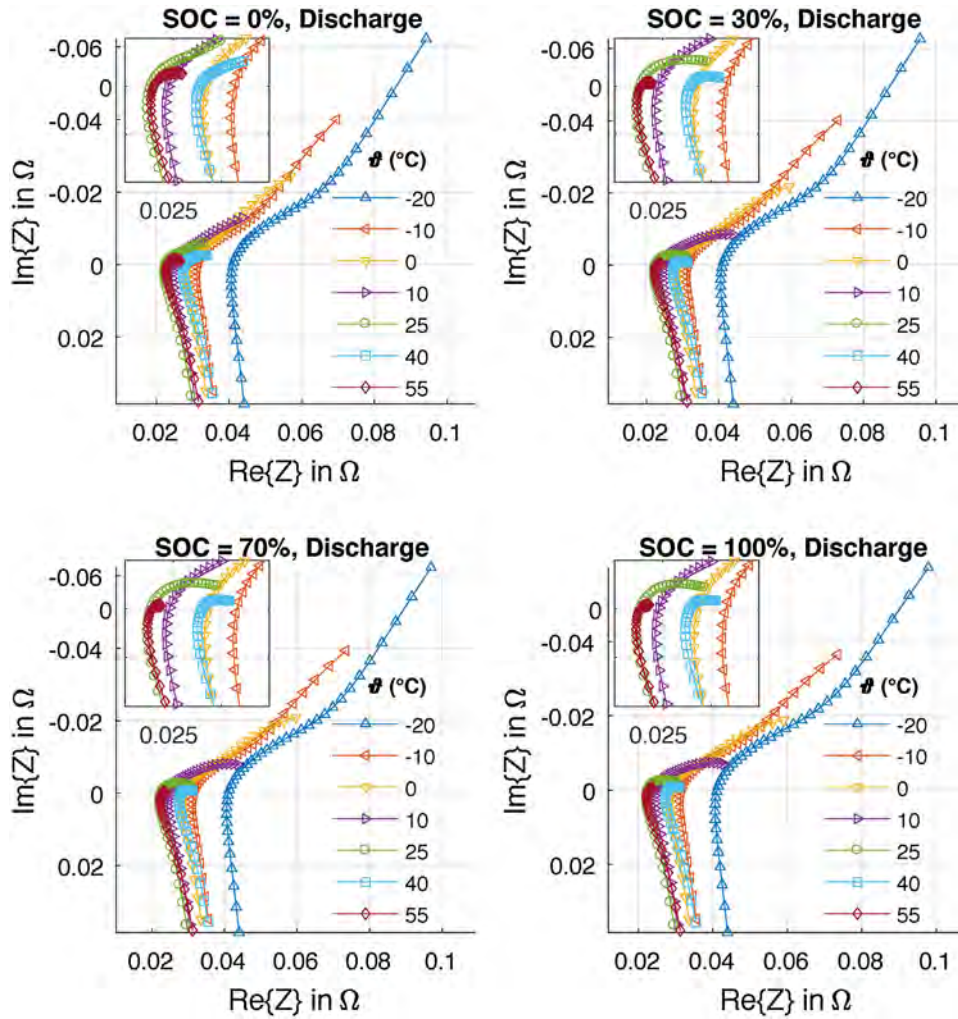
Fig. 5. Measurement results, summarized for same state of charge with a shown measurement range from $f_{EIS} \in [1\,Hz\ 100\,kHz]$.

Table 3
Analysis of descriptive parameters for the inductive behavior, taken from the measurements shown in Figs. 4 and 5.

Temperature in °C	−20	−10	0	10	20	40	55
f_{IS} in kHz	8.00	6.44	4.96	3.79	2.67	1.86	0.89
R_{IS} in mΩ	41.1	31.6	28.6	34.6	22.7	27.9	22.8
$\Delta R_{100\,kHz}$ in mΩ	3.4	4.4	5.5	6.4	7.4	8.2	9.1
$\Delta R_{1\,MHz}$ in mΩ	64.2	60.5	61.5	63.8	65.2	66.0	70.2
$L_{1\,MHz}$ in nH	57.5	50.3	49.8	51.5	51.1	48.3	51.7

Fig. 6 is designed for the first semicircle that is obviously exceeded with lower temperatures, as it can be seen in Fig. 5. All Nyquist plots used for parameterization have been cut off at $f_{co} = 100\,kHz$. At frequencies higher than f_{co}, the performance of the proposed model will decline. That is due to its structure as *RL*-circuits: Eventually, they are going to form a semicircle. However, this cannot be anticipated because the diagrams show an outward curvature for a prolonged band as it can be seen in Fig. 8 in which the full spectrum up to 1 MHz shown. The detail in the smaller picture shows the Nyquist curve up to f_{co}. In this wider
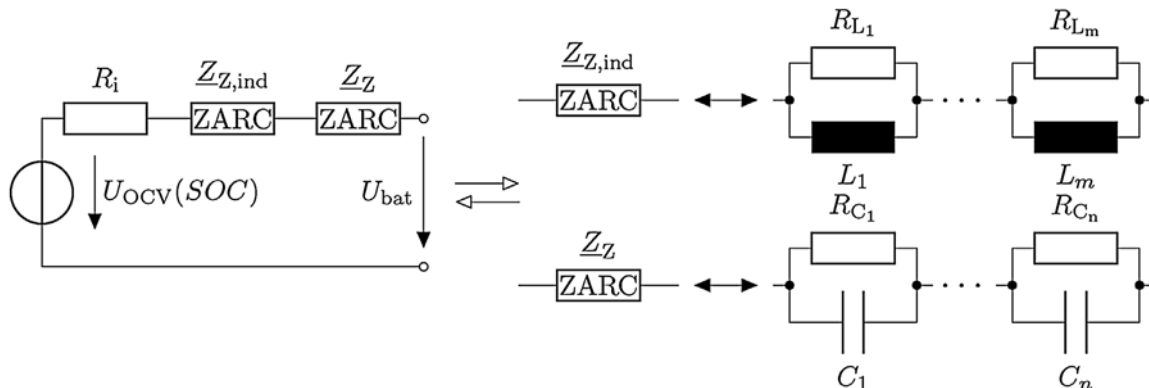

Fig. 6. Proposed circuit model. The inductive ZARC-element is modeled as *m RL*-circuits as the capacitive ZARC-element is approximated by *n RC*-circuits. They both form depressed semicircles in the positive and negative half-plane, respectively.
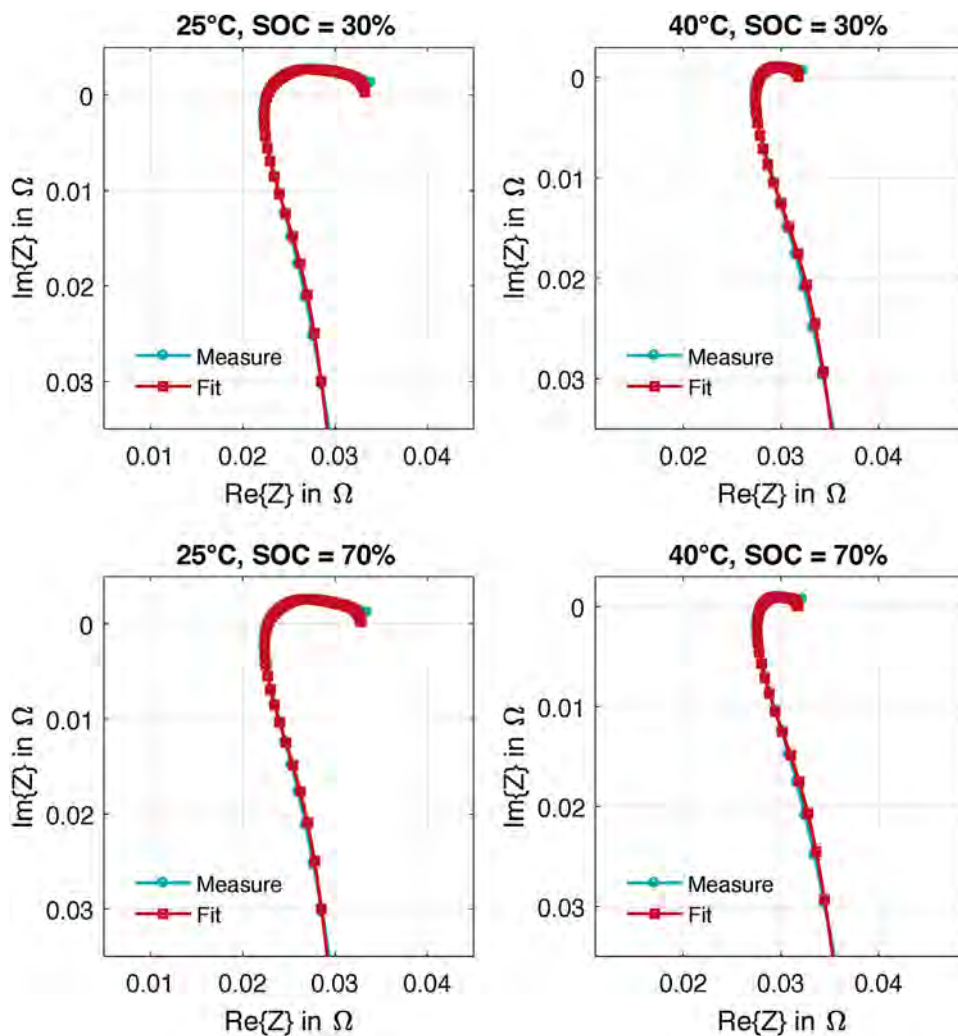
Fig. 7. Example plots with fitting results, based on the equivalent circuit in Fig. 6. The normalized root mean square errors are in the region of 0.3%.
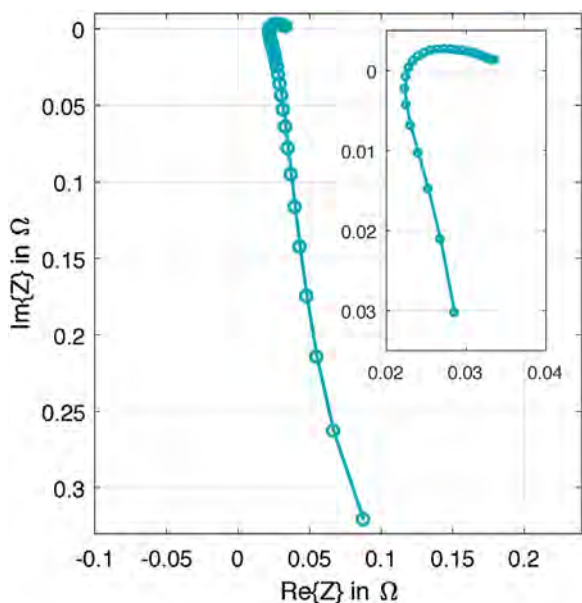

Fig. 8. Example plot showing the full measurement range up to 1 MHz. The more detailed view shows the Nyquist curve up to 100 kHz as all other figures before.

region, it is most likely that the impedance will mainly be affected by the skin effect [27]. This is going to be discussed deeper in the following Section 3.1.

3.1. Very high frequencies

The current collectors of the investigated batteries consist of copper and aluminum. As stated in [27], the skin effect is going to have a noticeable impact on the cell impedance, i.e. a rising resistance, at frequencies higher than several tens of kilohertz which is supported by Fig. 8. Therefore, it should be taken care of the skin effect if a model should be able to reproduce the cell's behavior at very high frequencies.

It is widely known that the electrical energy is transported by the electromagnetic field that propagates along the surface of a conductor and its diffusion into the conductor is directly linked to the electromagnetic properties of the conducting material and the field's frequency. As an approximate result of a diffusion equation, the penetration depth is often described by

$$\delta = \sqrt{\frac{2}{\omega\mu\kappa}}$$

(4)

with the angular frequency of the electromagnetic field ω, the permeability μ and the conductivity κ of the particular material. The penetration depth is seen as the section thickness of an equivalent circular conductor. Thus, δ can be linked to the geometrical description

$$R = \frac{l}{\kappa A} \qquad (5)$$

of a resistor with the length l and the cross section A. Since $A \sim \delta$, it follows that

$$R \sim \sqrt{\omega}. \qquad (6)$$

Based on the empirically motivated idea, that is presented in [31], the resistor R consists of an AC- and a DC-part that are added geometrically which leads to the resistance

$$R(\omega) = R_{DC} \sqrt{1 + x^2 \omega} \;=: R_{DC} \sqrt{1 + y\omega} \qquad (7)$$

with the newly introduced parameter y, with $[y] = s$. This formula can be used to simulate the skin effect. In order to compare this approach with Eq. (2), it has been combined with an inductance and the same ZARC element that is used in the previously discussed model with $n = 5$ as well. The full model equation follows accordingly as

$$\underline{Z}_{se}(\omega) = j\omega L + R_{DC} \sqrt{1 + y\omega} + \underbrace{\sum_{i=1}^{n} \frac{R_{C_i}}{1 + j\omega C_i R_{C_i}}}_{\underline{Z}_Z} \qquad (8)$$

and can be described with the equivalent circuit model that is depicted in Fig. 9.

A comparison between the skin effect model, the approximation chosen in the previous part with three *RL*-circuits and a more complex model with five *RL*-circuits is given in Fig. 10. All models have been fitted in the frequency region lower than 100 kHz. Moreover, the models based on *RL*-circuits have been given the same starting points for the fitting algorithm to ensure comparability. Obviously, a higher count of *RL*-circuits under the same conditions does not automatically lead to an approximation that is substantially more accurate. Until roughly $f_{co} = 100$ kHz both *RL*-model based curves are very close to the original measurement as it has also been shown in Fig. 7. In the same region of very high frequencies, the *RL*-circuit based models suffer from their mentioned design as a combination of inductive semicircles. The skin-effect based model can cope with this region much better. Yet, it cannot be ruled out that the deviation at the last point is connected to measurement errors.

Ultimately, there is no clear indication which model or a combination thereof should be used as they all have assets and drawbacks. One possible drawback of the skin effect model is that the knowledge of physical characteristics such as the conductivity or the permeability is often very limited and in most cases only a rough estimate would be available. Moreover, an impedance that is dependent on the square root of ω such as $R(\omega)$ would most likely be approximated by *RL*- or *RC*-circuits, respectively, which would further increase computational burden. In this work, the model based on *RL*-circuits is used since it is easy to parameterize and to implement although it is only viable in regions below 100 kHz. Yet, it is expected in any case that the harmonics of most switched power electronics should have declined far enough at the end of the model's frequency range as they normally decrease in orders of $1/n^2$ or at least $1/n$, as already illustrated in Fig. 1. In the next section, the chosen model is going to be validated with a simulation of a measured voltage response induced by an also measured
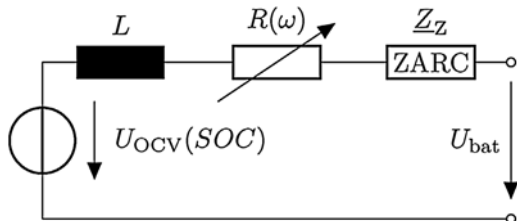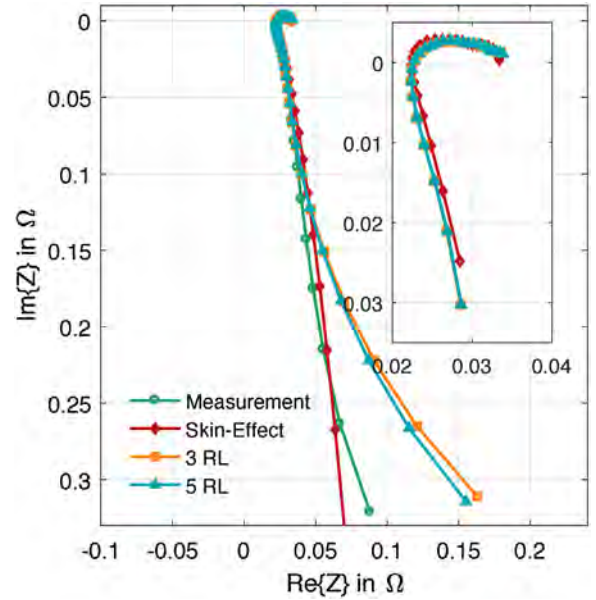
Fig. 10. Example plot showing the full measurement range up to 1 MHz and several fitting attempts with different models. Every model has been fitted in the standard frequency range [1 Hz 100 kHz]. This range is explicitly shown in detail in the upper right corner.

alternating charging and discharging current, respectively, that originates from a DC/DC-converter connected to the battery.

4. Validation and discussion

Regarding the premise that the proposed model should be able to represent a battery that is connected to power electronics and therefore under high-frequency stress due to current ripple, it seems likely to use an actual DC/DC-converter to conduct a convenient validation. Thus, a standard half bridge DC/DC-converter, as seen in many textbooks, such as [9], has been designed to charge and discharge an identical cylindrical 18650 LFP-battery since those have also been used to parameterize the model. The circuit's working principle is evaluated in Fig. 11 for both charging and discharging the battery. The battery is represented in the circuit by a SOC-dependent voltage source U_{OCV} that represents the OCV and an inner resistance R_e. By experience, such a reduced model suffices when it comes to designing a control law. With the battery being hard-wired to the low side of the converter, the differentiation between charge mode and discharge mode is solely determined by the switch between the voltage source that is used for charging the battery and the parallel *RC*-structure that is used for discharging it again. Aside from shutting down the circuit by sending a logical low signal to both MOSFETS at the same time and provoking a short-circuit by turning both transistors on at the same time, u and $\bar{u}$ indicate that antipodal switching is used to control the circuit with a pulse width modulated (PWM) signal. Based on the current direction and whether the battery is charged or discharged an overall four conduction modes, that are marked by the blue solid lines and the yellow dashed lines in Fig. 11, can take effect and partly charge or discharge the inductance. As this is highly influenced by the PWM, the current i_L and ultimately the battery current becomes controllable. Without going into further detail, current control is done by an observer based state-feedback control loop that is able to asymptotically follow a reference value even under pervasive parameter perturbations.

The most important parameters of the DC/DC-converter that has been built to validate the model are listed in Table 4. The resistive load, the switching frequency and die inductor are designed in regard to the voltage source so that the inductor current ripple is in orders of 40% compared to the mean discharge or charge current, respectively.

Fig. 9. Equivalent circuit for the skin effect model. The resistance stands for $R(\omega) = R_{DC} \sqrt{1 + y\omega}$ and therefore not a pure ohmic resistance, obviously.
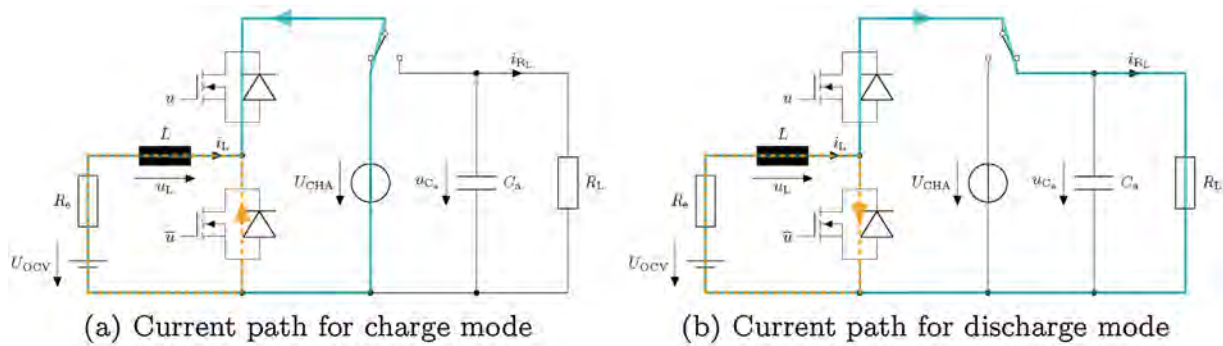
Fig. 11. Basic schematic of a half-bridge DC/DC-converter to illustrate the working principle. The converter connects a source for charging or a resistive load with a smoothing capacitor for discharging with the battery. The current paths are shown as arrows for each switch setting.

Table 4
Main attributes of the DC/DC-converter, shown in Fig. 11.

Value	Symbol	Quantity
Input voltage	U_{CHA}	12 V
Smoothing capacitor	C_a	1 mF
Inductance	L	860 µH
Switching frequency	f_S	5 kHz
Resistive load	R_L	16 Ω

Standard low series resistance *n*-channel power MOSFETS with internal body diodes have been used. As the voltage source and the load are connected to the high side of the converter, the battery is found on the low side and in series with the inductor. Its current is the controlled state variable with its mean value being the desired value so that an immediate influence on the charge and discharge current, respectively, is established.

With the converter being set, a LFP-battery with parameters as in Table 1 has been cycled with a mean charge current of $I_{CHA} = 2.5$ A and a mean discharge current of $I_{DCH} = -2.5$ A. At arbitrary points in time the battery current and its voltage have been measured with a "Tektronix TBS1064" digital oscilloscope. A shielded "Keysight 1146B" current transducer with a bandwidth up to 100 kHz has been used to measure the current whereas a "Testec SI 9001" differential voltage probe with a frequency range up to 25 MHz has been used to detect the cell's voltage.

An excerpt of the validation results is shown in Fig. 12 during discharge on the left side as well as during charge on the right side of the picture. In the first row, the current curve and its high frequency ripple with an amplitude of roughly 1 A is observable. As stated before, the current ripple has been designed to be around 40%. Yet, it is not possible in this basic converter design with a fixed frequency to obtain ripple at all operation points, for it is dependent on the load which constantly changes if the cell is charged or discharged with a constant mean current.

In the second row, the current harmonics are shown. The cropped line at the zero order harmonic is the DC-part, thus it reaches the mean charge or discharge current amplitude which is set here to $I_{CHA,DCH} = \pm 2.5$ A. It can also be seen, that substantial peaks in current harmonics all arise at multiples of the switching frequency which shows that the current is periodical and symmetrical. As anticipated, a triangular current's harmonics decline in orders of $1/n^2$ so that there is not any measurable excitation to be expected at frequencies higher than 100 kHz. Therefore, it suffices to parameterize the model up to 100 kHz if the influence of the current ripple shall be simulated. If the battery's behavior under EMI stress was to be examined, a more sophisticated approach such as a complex transmission line model as discussed in [19,20] or a model that includes the skin effect, see Section 3.1.

In the last row of Fig. 12, the measured voltage response is shown as a solid line. On top of it, the simulated response is given. Except for

random spikes that are most likely linked to EMI effects in the measurement chain and therefore cannot be reproduced appropriately by the developed model, a simple optical comparison suggests a well working simulation. Calculating the normalized root mean square error, see Eq. (3), confirms the optically gotten assumption as the error remains below 0.2% for both charge and discharge.

Fig. 13 shows an excerpt of the battery's voltage response while charging, shown on the right side of Fig. 12. As before, the measured voltage and simulation result of the high frequency model with three *RL*-circuits is shown in the colors and line pattern as before. Additionally, the dash-dotted yellowish curve represents the same simulation. However, the *RL*-circuits have been abandoned and only the pure ohmic resistance remains to represent the high frequency behavior. A small but distinct variation shows that the *RL*-circuits are able to deal better with the steep ripple. However, using only the resistance can still lead to satisfactory results in terms of short time frames if highest accuracy is not crucial [32]. This could be the case if a fast, yet robust control algorithm was implemented as it has been the case for the half-bride test circuit used to validate the model. Additionally, exchanging the *RL*-circuits with an inductance leads to severe overshoots due to the direct feed through of EMI. Thus, this variant has not been investigated further.

Consequently, it is concluded that the proposed model gives satisfying results and is a comprehensive addition to common equivalent circuit models that do not include inductive behavior, not just as an opportunity to give a more detailed description of a cell's behavior to improve simulation results overall but as a useful tool for designing battery power systems that imply an interconnection of batteries and fast switching power electronics.

5. Conclusion

A battery model to represent the behavior under high frequency excitation, e.g. induced by the current ripple of power electronics, has been proposed. It is based on an equivalent circuit that consists of an inductive constant phase element that is approximated by an almost arbitrary number of *RL*-circuits. In this work, using three *RL*-circuits has shown good results continuously within a frequency range up to 100 kHz which should suffice for a broad variety of applications. Moreover, a capacitive constant phase element has been added to take mid frequency effects down to 1 Hz into account so that the simulation can remain accurate as the inductive behavior is affected by the capacitive one and vice versa [18]. It is convenient to also model the capacitive CPE with corresponding *RC*-circuits. To obtain the parameters of the model, electrochemical impedance measurements have been conducted in a frequency range from 1 Hz to 1 MHz. However, the data has been cropped at 100 kHz to achieve higher accuracy in the most important range for a lot of power electronic applications, see Fig. 10 and the middle part of graphic Figure 12. The equivalent circuit has been implemented into *MATLAB/Simulink* as a block diagram that has
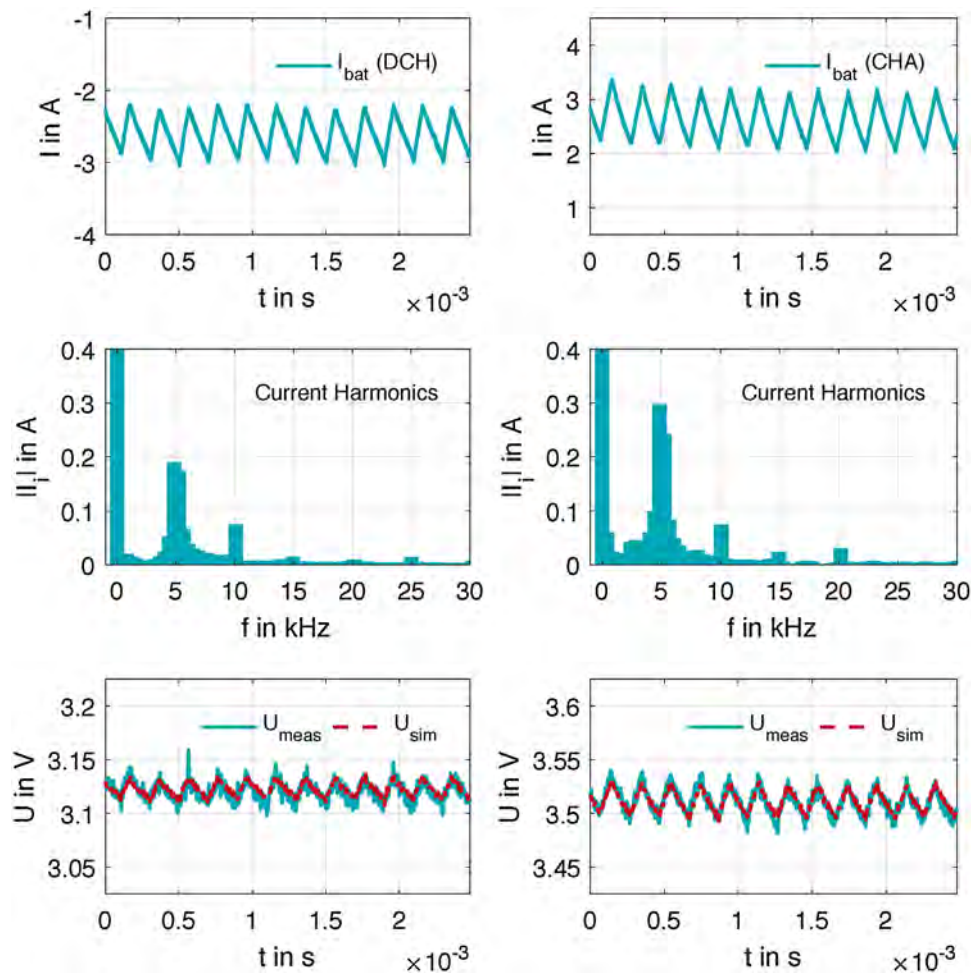
Fig. 12. Simulation results for discharging on the left side and charging on the right side. The measurements have been recorded with a digital oscilloscope.
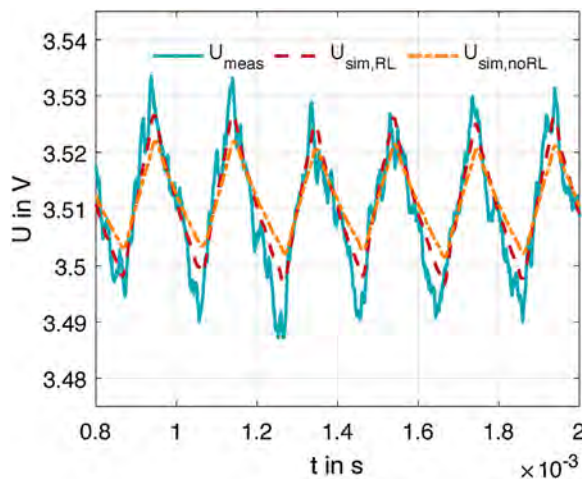

Fig. 13. Exemplatory comparison between a simulation with three *RL*-circuits (dashed red line) and a simulation without any inductive part (dash-dotted yellow line). It has to be noted that both the input current and the measured voltage have been filtered to a large extend to tone down the voltage's noise, thus making the desired effect more visible. (For interpretation of the references to color in this figure legend, the reader is referred to the web version of this article.)

been given a battery current with severe ripple, originating from a half bridge DC/DC-converter, to validate its calculated voltage response. The results clearly indicate that the model delivers the anticipated

results so that it might be considered to improve commercial battery models in battery energy systems such as electric vehicles or larger scale stationary battery systems, for they all have their battery systems connected to power electronics that induce high frequency ripple. At the present day, it is not yet well known, how the aforementioned current ripple affects the battery performance and especially if there is any severe effects on battery aging. A model like the one that is introduced in this work can play a key role in further investigating battery systems and answer questions that have arisen in this context.

References

[1] IRENA, Electricity Storage and Renewables: Costs and Markets to 2030, International Renewable Energy Agency, 2017.

[2] IEA, Global EV Outlook: Two Million and Counting, International Energy Agency, 2017.

[3] R.H. Lasseter, Microgrids, 2002 IEEE Power Engineering Society Winter Meeting. Conference Proceedings (Cat. No. 02CH37309), vol. 1 (2002) 305–308, http://dx.doi.org/10.1109/PESW.2002.985003.

[4] B. Diouf, R. Pode, Potential of lithium-ion batteries in renewable energy, Renew. Energy 76 (Suppl. C) (2015) 375–380, http://dx.doi.org/10.1016/j.renene.2014.11.058.

[5] D. Varajao, R.E. Araujo, L.M. Miranda, J.P. Lopes, N.D. Weise, Control of an isolated single-phase bidirectional ac–dc matrix converter for v2g applications, Electr. Power Syst. Res. 149 (Suppl. C) (2017) 19–29, http://dx.doi.org/10.1016/j.epsr.2017.04.004.

[6] M. Yilmaz, P.T. Krein, Review of battery charger topologies, charging power levels, and infrastructure for plug-in electric and hybrid vehicles, IEEE Trans. Power Electron. 28 (5) (2013) 2151–2169, http://dx.doi.org/10.1109/TPEL.2012.2212917.

[7] W. Kempton, J. Tomic, Vehicle-to-grid power fundamentals: calculating capacity and net revenue, J. Power Sources 144 (1) (2005) 268–279 doi:https://doi.org/10.1016/j.jpowsour.2004.12.025.

[8] W. Kempton, J. Tomic, Vehicle-to-grid power implementation: from stabilizing the grid to supporting large-scale renewable energy, J. Power Sources 144 (1) (2005) 280–294, http://dx.doi.org/10.1016/j.jpowsour.2004.12.022.

[9] R.W. Erickson, D. Maksimovic, Fundamentals of Power Electronics vol. 2, Kluwer Academic Publishers, 2004.

[10] W. Waag, C. Fleischer, D.U. Sauer, Critical review of the methods for monitoring of lithium-ion batteries in electric and hybrid vehicles, J. Power Sources 258 (Suppl. C) (2014) 321–339, http://dx.doi.org/10.1016/j.jpowsour.2014.02.064.

[11] E. Barsoukov, J.R. Macdonald, Impedance Spectroscopy vol. 2, Wiley-Interscience, 2005.

[12] S. Buller, M. Thele, R.W.A.A.D. Doncker, E. Karden, Impedance-based simulation models of supercapacitors and Li-ion batteries for power electronic applications, IEEE Trans. Ind. Appl. 41 (3) (2005) 742–747, http://dx.doi.org/10.1109/TIA.2005.847280.

[13] SMG, M. Nikdel, Various battery models for various simulation studies and applications, Renew. Sustain. Energy Rev. 32 (Suppl. C) (2014) 477–485 doi:https://doi.org/10.1016/j.rser.2014.01.048.

[14] A. Fotouhi, D.J. Auger, K. Propp, S. Longo, M. Wild, A review on electric vehicle battery modelling: from lithium-ion toward lithium-sulphur, Renew. Sustain. Energy Rev. 56 (Suppl. C) (2016) 1008–1021, http://dx.doi.org/10.1016/j.rser.2015.12.009.

[15] M. Uno, K. Tanaka, Influence of high-frequency charge-discharge cycling induced by cell voltage equalizers on the life performance of lithium-ion cells, IEEE Trans. Vehic. Technol. 60 (4) (2011) 1505–1515, http://dx.doi.org/10.1109/TVT.2011.2127500.

[16] A. Rahmoun, A. Armstorfer, J. Helguero, H. Biechl, A. Rosin, Mathematical modeling and dynamic behavior of a lithium-ion battery system for microgrid application, 2016 IEEE International Energy Conference (ENERGYCON) (2016) 1–6, http://dx.doi.org/10.1109/ENERGYCON.2016.7513977.

[17] J. Wang, K. Zou, C. Chen, L. Chen, A high frequency battery model for current ripple analysis, 2010 Twenty-Fifth Annual IEEE Applied Power Electronics Conference and Exposition (APEC) (2010) 676–680, http://dx.doi.org/10.1109/APEC.2010.5433598.

[18] H. Witzenhausen, Elektrische batteriespeichermodelle: Modellbildung, parameteridentifikation und modellreduktion (Ph.D. thesis), RWTH Aachen, Aachen, 2017, http://dx.doi.org/10.18154/RWTH-2017-03437.

[19] S. Jeschke, M. Maarleveld, J. Baerenfaenger, H. Hirsch, S. Tsiapenko, C. Waldera, M. Obholz, Development of a passive impedance network for modeling electric vehicle traction batteries for EMI measurements, 2017 International Symposium on Electromagnetic Compatibility – EMC EUROPE (2017) 1–6, http://dx.doi.org/10.1109/EMCEurope.2017.8094615.

[20] S. Schindler, M.A. Danzer, Influence of cell design on impedance characteristics of cylindrical lithium-ion cells: a model-based assessment from electrode to cell level, J. Energy Storage 12 (Supplement C) (2017) 157–166, http://dx.doi.org/10.1016/j.est.2017.05.002.

[21] M. Guo, R.E. White, Mathematical model for a spirally-wound lithium-ion cell, J. Power Sources 250 (Suppl. C) (2014) 220–235, http://dx.doi.org/10.1016/j.jpowsour.2013.11.023.

[22] M. Petzl, M.A. Danzer, Advancements in OCV measurement and analysis for lithium-ion batteries, IEEE Trans. Energy Convers. 28 (3) (2013) 675–681, http://dx.doi.org/10.1109/TEC.2013.2259490.

[23] F.M. Kindermann, A. Noel, S.V. Erhard, A. Jossen, Long-term equalization effects in Li-ion batteries due to local state of charge inhomogeneities and their impact on impedance measurements, Electrochim. Acta 185 (Suppl. C) (2015) 107–116, http://dx.doi.org/10.1016/j.electacta.2015.10.108.

[24] E. Gileadi, Physical Electrochemistry vol. 1, Wiley-VCH, 2011.

[25] D. Andre, M. Meiler, K. Steiner, H. Walz, T. Soczka-Guth, D. Sauer, Characterization of high-power lithium-ion batteries by electrochemical impedance spectroscopy. II. Modelling, J. Power Sources 196 (12) (2011) 5349–5356, http://dx.doi.org/10.1016/j.jpowsour.2010.07.071.

[26] A. Seaman, T.S. Dao, J. McPhee, A survey of mathematics-based equivalent-circuit and electrochemical battery models for hybrid and electric vehicle simulation, J. Power Sources 256 (2014) 410–423, http://dx.doi.org/10.1016/j.jpowsour.2014.01.057.

[27] A. Jossen, Fundamentals of battery dynamics, J. Power Sources 154 (2) (2006) 530–538, http://dx.doi.org/10.1016/j.jpowsour.2005.10.041.

[28] P. Osswald, S. Erhard, A. Noel, P. Keil, F. Kindermann, H. Hoster, A. Jossen, Current density distribution in cylindrical Li-ion cells during impedance measurements, J. Power Sources 314 (2016) 93–101, http://dx.doi.org/10.1016/j.jpowsour.2016.02.070.

[29] L.W. Juang, P.J. Kollmeyer, A.E. Anders, T.M. Jahns, R.D. Lorenz, D. Gao, Investigation of the influence of superimposed ac current on lithium-ion battery aging using statistical design of experiments, J. Energy Storage 11 (2017) 93–103, http://dx.doi.org/10.1016/j.est.2017.02.005.

[30] R.E. Gutiérrez, J.M. Rosario, J.T. Machado, Fractional order calculus: Basic concepts and engineering applications, Math. Probl. Eng. 2010 (2010) 1–19, http://dx.doi.org/10.1155/2010/375858.

[31] E. Hoene, S. Guttowski, R. Saikly, W. John, H. Reichl, RF-properties of automotive traction batteries, 2003 IEEE International Symposium on Electromagnetic Compatibility, 2003, EMC'03, vol. 1 (2003) 425–428, http://dx.doi.org/10.1109/ICSMC2.2003.1428282.

[32] SMG, M. Nikdel, Various battery models for various simulation studies and applications, Renew. Sustain. Energy Rev. 32 (2014) 477–485, http://dx.doi.org/10.1016/j.rser.2014.01.048.